Impact of the Nocturnal Low-Level Jet and Orographic Waves on Turbulent Motions and Energy Fluxes in the Lower Atmospheric Boundary Layer

Sayahnya Roy, Alexei Sentchev, François G Schmitt, Patrick Augustin, Marc Fourmentin

Impact of the Nocturnal Low-Level Jet and Orographic Waves on Turbulent Motions and Energy Fluxes in the Lower Atmospheric Boundary Layer

Sayahnya Roy[1,2] • Alexei Sentchev[1] • François G. Schmitt[1] • Patrick Augustin[2] • Marc Fourmentin[2]

Received: DD Month YEAR/ Accepted: DD Month YEAR/ Published online: DD Month YEAR

Abstract The nocturnal low-level jet (LLJ) and orographic (gravity) waves play an important role in the generation of turbulence and pollutant dispersion and can affect the energy production by wind turbines. Additionally, gravity waves have an influence on the local mixing and turbulence within the surface layer and the vertical flux of mass into the lower atmosphere. On 25 September 2017 during a field campaign, a persistent easterly LLJ and gravity waves are observed simultaneously in a coastal area in the north of France. In the present study, an attempt is to explore the variability of the wind speed, turbulent eddies, and turbulence kinetic energy in the time-frequency and space domain using an ultrasonic anemometer and a scanning wind lidar. The results reveal a significant enhancement of the turbulence kinetic energy dissipation (by ~50%) due to gravity waves in the LLJ shear layer (below the jet core) during the period of wave propagation. Large values of zonal and vertical components of the shear stress (~|0.4| and ~|1.5| m^2 s^{-2} respectively) are found during that period. Large size eddies (~110 to 280 m), matching high-speed wind regime, are found to propagate the momentum downward. This enhances the downward mass transport from the LLJ shear layer to the roughness layer. Furthermore, these large-scale eddies are associated with the crests while comparatively small-scale eddies are associated with the troughs of the gravity wave.

✉ Sayahnya Roy
email. sayahnya1110@gmail.com

[1] Univ. Littoral Cote d'Opale, Univ. Lille, CNRS, UMR 8187, LOG, Laboratoire d'Océanologie et de Géosciences, F 62930 Wimereux, France.

[2] Univ. Littoral Côte d'Opale, EA 4493, LPCA, Laboratoire de Physico-Chimie de l'Atmosphère, 59140, Dunkerque, France.

Keywords Lidar measurements • Low-level Jet • Probability Density Function • Sonic Anemometer • Turbulent eddies

1 Introduction

After sunset, strong wind acceleration at the altitude 100–200 m above ground level (a.g.l.) is frequently observed. This phenomenon, known as the nocturnal low-level jet (LLJ), is defined as concentrated airflow within the atmospheric boundary layer (ABL) over sea or land surface (Banta et al. 2003). The maximum jet velocity is influenced by several factors such as horizontal temperature gradients, orographic features, elevated turbulence level, etc. (Birgitta 1998; Kallistratova et al. 2013). Moreover, LLJs can be formed by synoptic cold fronts, thunderstorm gustfronts, drainage-flow fronts, and sea-breeze fronts. Bowen (1996), Droegemeier and Wilhelmson (1987), and Darby et al. (2002) characterized the LLJ profile after the front within a cold-air layer. Also, Whiteman et al. (1997) provided a description of an LLJ generated at a cold-air front by large-scale density currents. Furthermore, nocturnal LLJs are found to be generated by atmospheric pressure gradients and baroclinitity (Hoecker 1963; Bonner 1968; Mitchell et al. 1995; Zhong et al. 1996), which has been widely studied to detect its influence in severe weather conditions (Stensrud 1996). Prabha et al. (2008) showed that a high wind speed may occur not only in the vicinity of the ABL top, but also in the shear layer, i.e. from 10 to 100 m a.g.l. Kaimal and Finnigan (1994) noted that the maximum turbulence exchange occurs between a canopy and the atmosphere, due to the coherent wind structures of the size of the canopy. Further, Raupach et al. (1996) documented large-scale eddies generated by the interaction of the wind with a large canopy (large surface roughness). They observed a modulation of the eddies's size by turbulence, and showed that flow instabilities are governed by the wind velocity shears.

Wind velocity fluctuations near the surface are involved in a cyclic process. In this process the wind propagating slowly in the surface layer can be accelerated rapidly within the outer layer (the uppermost 90% of the ABL, according to Rotach and Calanca 2015). This is known as a "turbulent bursting event". The downbursts due to the large roughness heights were observed by Hunt and Durbin (1999) within the lower layer. Furthermore,

Smedman et al. (2004) showed that this type of phenomenon could be observed in the presence of a LLJ tied to intense shear.

In the present study, an undulating motion generated by gravity or orographic waves collocated with a LLJ has been observed in the lower ABL. Hoffmann et al. (2013) reported that the source of many gravity waves is related to orographic features. It was also documented in several studies (e.g., Fritts and Nastrom 1992; Eckermann and Vincent 1993; Plougonven and Teitelbaum 2003) that low-frequency gravity waves occurred in the area surrounding jets and fronts, particularly in the upper troposphere regions. Those large-scale gravity waves are known as inertia-gravity waves (Uccellini and Koch 1987; Guest et al. 2000).

Gravity-wave motions are observed in the free atmosphere when the Brunt–Väisälä period of oscillations in positively stratified air changes to the inertial period. Mountain-waves are one of the specific cases. In the lower troposphere, wind blowing over small hills starts oscillating vertically. The Coriolis force creates individual elliptic shape in the plane of wind propagation and perhaps gives rise to low frequency, horizontal, inertia gravity waves. These waves are frequently observed at mid-latitudes, especially in the lower atmosphere (Vaughan and Hooper 2015). Recently, Wei et al. (2017) demonstrated that events with small wind speed, large-scale motions (e.g., gravity waves, mesoscale disturbances, or synoptic-scale variability) were capable of generating small- to large-scale turbulent eddies.

Recent studies have focused on assessing ABL phenomena, such as LLJ or gravity waves, individually (Teixeira 2014; Soufflet et al. 2019). Also, some studies focused on the low-level gravity waves (Tepper 1950; Abdullah 1955). They revealed that low-level gravity waves produce vertical motions, which are capable of forming convective storms. Recently, Du and Chen (2019) studied the mesoscale impacts of wavelike disturbances of double LLJs on convection initiation mechanisms. This recent research highlighted the need to improve understanding of the relationship between gravity waves and high frequency turbulence in the lower ABL. The gap of knowledge is related to the insufficient simultaneous observations of both phenomena.

In the present study, we focus on assessing the turbulence characteristics (such as turbulence kinetic energy and momentum fluxes) in the lower ABL, at 10 m height above

the ground, and their modulation by gravity waves propagating at large distance from the ground. We also quantify the distribution of turbulent eddies in time–space and frequency domain and identify the direction of kinetic energy transfer generated by turbulent eddies toward the roughness layer (extending up to a few metres from the ground level). Moreover, we assess the variability of turbulence kinetic energy (TKE) dissipation, turbulence length scales, momentum fluxes, and turbulent bursting events in the presence of a gravity wave collocated with a LLJ. The paper is organized as follows. In Sect. 2, we present the data and the methods of analysis. Section 3 contains the discussion of our results. Section 4 concludes the study and gives some implications of the observed large-scale motions in the ABL on turbulence near the ground.

2 Data and Methods

2.1 Study Site and Wind Measurements

In the frame of the EMPATIE project (Multiscale study of turbulent atmospheric phenomena and their influences on wind power), an atmospheric mobile unit (UMA) was deployed on 25 September 2017 (Fig. 1), near the seashore at Boulogne-sur-Mer (France). Wind profiles were measured using a scanning Doppler wind lidar (LEOSPHERE, Windcube WLS 100) and a sonic anemometer (model USA-1, Metek GmbH). The pulsed Doppler lidar operates at 1543 nm and uses a heterodyne technique to measure the Doppler shift of laser radiation backscattered by the aerosols (Augustin et al. 2020). The wind speed is estimated from the Doppler shift at different vertical levels. More technical details are given by Ruchith et al. (2015) and Kumer et al. (2016). During the experiment, the lidar performed, consecutively, range–height indicator (RHI) scans along the north–south and east–west and Doppler beam swinging (DBS) techniques (Kumer et al. 2016). The DBS technique has been used to determine the temporal evolution of horizontal wind velocity profiles. The RHI scans allowed us to observe the vertical and spatial structure of the lower troposphere from the ground to few kilometres with a blind zone of 100 m around the lidar. Moreoever, vertical profiles from RHI scans have been used to measure directly the vertical wind speed. The measurement strategy was constituted of two 180° RHI scans along east–west and south–north axes with 1° resolution (3 min duration per each RHI scan), and a 75° elevation DBS technique (1 min duration).

Two particular periods of lidar observations were considered: the first period, P-I, from 1800 to 0000 UTC (from sunset to midnight) and the second period, P-II, from 0000 to 0600 UTC (from midnight to sunrise). During P-I, a LLJ collocated with gravity waves was observed in the lower troposphere. However, both phenomena (the LLJ and gravity waves) dissipated during P-II.

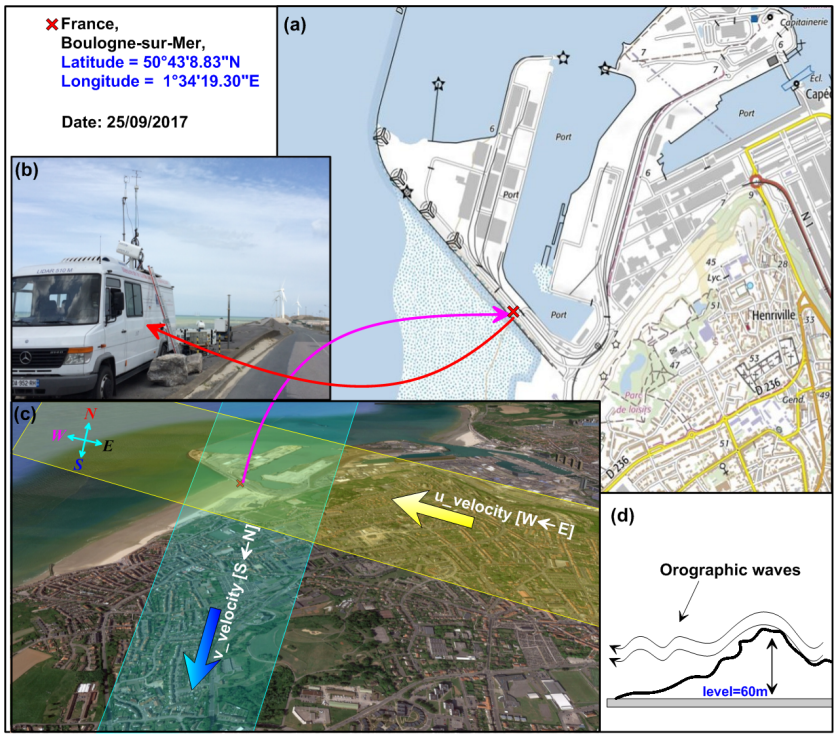

Fig. 1 Location and period of measurements in Boulogne-sur-Mer. (a) Map of topographical levels, (b) mobile atmospheric data acquisition unit of the University of Littoral Côte d'Opale located on the seashore (red cross) equipped with a sonic anemometer and lidar (Windcube WLS 100), (c) satellite image of the study area with the indication of wind directions, (d) schematic of orographic waves due to easterly wind over elevated topography

Lidar measurements were complemented by the data from an ultrasonic anemometer operating at 10-Hz (from 1800 to 0600 UTC) and provided three components of the wind velocity and temperature variations. This sonic anemometer was deployed in the roughness layer on a 7 m mast in the blind zone of the lidar. Indeed, the lidar near-field is affected by an incomplete overlap between the laser beam and the field-of-view of a telescope corresponding to the blind zone of the lidar. No data could be recorded in this zone. The first gate was 100 m and the along-beam spatial resolution was 50 m.

2.2 Methodology

The velocity components u, v, and w of the wind flow (measured by ultrasonic anemometer) are decomposed into a mean part and fluctuating part as

$$u = \overline{u} + u', v = \overline{v} + v' , w = \overline{w} + w' , \quad (1)$$

where u, v, w are three components of the instantaneous velocity vector, $\overline{u}, \overline{v}, \overline{w}$ are 10-min averaged components and u', v', and w' are the corresponding velocity fluctuations. Note that the positive zonal component u represents the wind blowing from the west, the positive meridional component v characterizes the wind blowing from the south, and the positive vertical component w describes the wind blowing upward.

The time-averaged Reynolds shear stress components are defined as

$$R_{uv} = -\overline{u'v'};\ R_{uw} = -\overline{u'w'};\ R_{vw} = -\overline{v'w'} , \quad (2)$$

and the turbulence kinetic energy (*TKE*) can be written as

$$TKE = \frac{1}{2}(\overline{u'^2} + \overline{v'^2} + \overline{w'^2}). \quad (3)$$

To understand the distribution of the turbulent eddy structures in the frequency domain and the maximum energy-carrying frequency of the wind velocity signal, spectral analysis was performed using the FFT (fast Fourier transform) algorithm. The turbulence dissipation rate (ε) is estimated from instantaneous wind measurements by sonic anemometer using two different methods: the energy spectra method and the second-order structure function method. The velocity spectrum, which satisfies the -5/3 slope within the inertial subrange (Kolmogorov 1941), can be defined as

$$E(k) = \alpha\varepsilon^{2/3}k^{-5/3} , \quad (4)$$

where k is the wavenumber and α is the Kolmogorov constant ($\alpha = 0.52$). The conversion of the spectrum from wavenumber to frequency domain is based on Taylor's frozen turbulence hypothesis (Taylor 1935) providing

$$k = 2\pi f/\overline{U} , \quad (5)$$

where $\overline{U}$ is the mean wind speed. The turbulence dissipation rate is computed using one-dimensional velocity spectrum $S_u(f)$ in the inertial subrange (Champagne et al. 1977) as

$$\varepsilon = \frac{2\pi}{\overline{U}}\left(\frac{f^{5/3}S_u(f)}{\alpha}\right)^{3/2} . \quad (6)$$

158 Further, velocity increments within the inertial subrange can be conveyed as the second-
159 order structure function (SF2) using Kolmogorov's hypothesis, and it can be
160 interconnected to ε as

$$SF2_u(r) = \overline{[u(x+r) - u(x)]^2} = \frac{1}{\alpha}\varepsilon^{2/3}r^{2/3}\,, \tag{7}$$

161 where r represents the spatial separations within the inertial subrange, which can be also
162 expressed as temporal velocity increments by applying Taylor's frozen turbulence
163 hypothesis. Finally, ε can be calculated (similar to Bodini et al. 2018) from the second-
164 order structure function as

$$\varepsilon = \frac{1}{\bar{U}\tau}[\alpha SF2_u(\tau)]^{3/2}\,, \tag{8}$$

165 where $SF2_u(\tau)$ is the second-order structure function for velocity u with respect to
166 temporal increments τ. The turbulent length scale (L) is computed as

$$L = \frac{TKE^{3/2}}{\varepsilon}\,. \tag{9}$$

167 All these quantities are used in the subsequent analysis for assessing the wind
168 variability in the roughness layer modulated by gravity-wave interaction with the LLJ.
169 Reynolds shear stress depicts the direction of the momentum flux affected by a LLJ
170 collocated with gravity waves. Further, the variability of TKE and ε shows the modulation
171 of the overall energy by large-scale motions in the ABL (LLJ and the gravity waves). Time
172 variability in wind energy is related to eddy motions of length scale given by L. Turbulent
173 energy propagates three-dimensionally and the dominant direction of an energy flux can
174 be quantified by the skewness. Turbulence bursts establish variations in the momentum
175 exchanges, demonstrated by the probability density distributions and joint distributions of
176 velocity fluctuations. In this study, quadrant analysis is used to demonstrate the impact of
177 gravity waves on the direction of high- and low-speed eddy propagation within the
178 roughness layer.
179

180 3 Discussions of the Results

181 3.1 Temporal Variations of Wind

182 The horizontal wind direction, and horizontal and vertical wind speed in the lower
183 atmosphere observed by Doppler lidar are shown in Fig. 2a, b. In general, northerly wind
184 is observed above the altitude 600 m from 2000 to 0600 UTC (wind speed 1 m s^{-1} to 4 m

s^{-1}). However, below this altitude and above the ground, the wind direction changes to easterly for the whole period of observation. Large range of horizontal (3.5 to 8 m s^{-1}) and vertical (-0.6 to 0.3 m s^{-1}) wind speed variation are observed below 500 m during P-I. During P-II (after 0000 UTC), the wind speed decreases in the whole layer covered by observations.

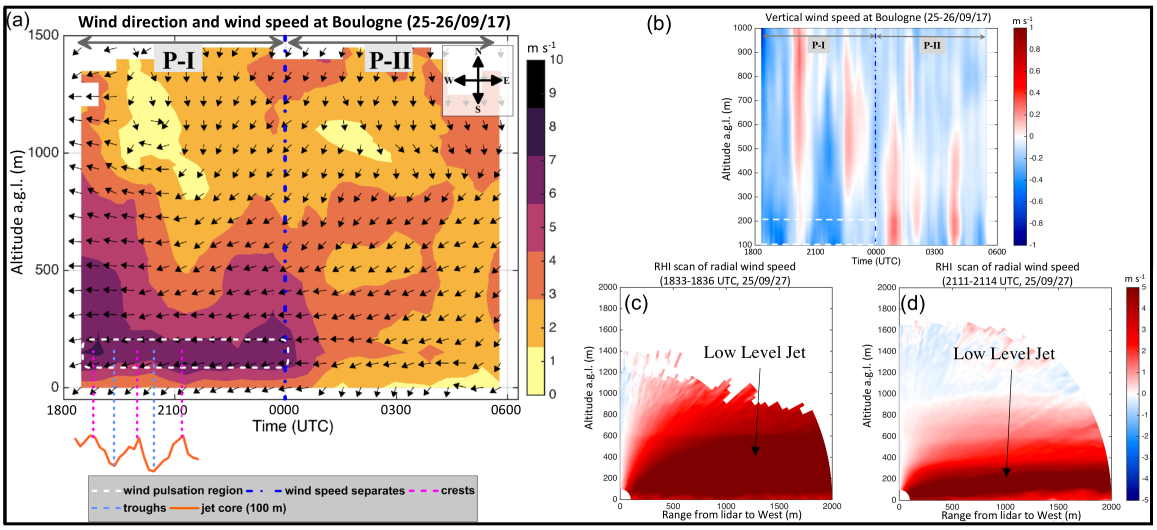

Fig. 2 Time–height cross-section of (a) horizontal wind direction (arrows) and speed (colour scale) and (b) vertical wind speed observed in Boulogne-sur-Mer on 25/09/17. Downward and leftward arrows represent northerly wind and easterly wind, respectively. The orange line (bottom of the figure) shows undulating patterns of maximum wind speed at 100 m. The white dashed time window corresponds to the main location of the jet core observed. RHI scan of radial wind speed toward the sea at (c) 1833 UTC and (d) 2111 UTC illustrating the LLJ phenomenon (positive values indicate flow away from lidar).

In Fig. 2a, a blue dash-dot line separates this high-speed and low-speed wind periods in the lower troposphere (<500 m). During P-I and in the lower troposphere, LLJ is clearly detected by the lidar (Figs. 2c, d). The RHI scan of radial wind speed toward the sea, performed one hour after the sunset, shows a 500 m thick LLJ (Fig. 2c), which becomes thinner and decouples from the ground at about 1930 UTC (Fig. 2d). However, during the day and before the LLJ occurrence, surface wind speed was relatively low (between 2 and 4 m s^{-1}) and the wind direction was mainly easterly (not shown). Although during the night, the wind speed was relatively hight (> 6 m s^{-1}), it decreased considerably from 6 m s^{-1} down to 2 m s^{-1} after the sunrise at about 530 UTC (25/09/2017). The frictional force caused by the turbulence associated with the heated ground during the day can decrease the wind

speed. Conversely, at the sunset (about 1730 UTC), the daytime frictional force shut down (due to the collapse of convective turbulence) and consequently the air mass accelerates generating the LLJ. Figure 2d represents a typical radial wind speed RHI scan obtained after 1930 UTC and illustrates the shear located above and below the height of the LLJ maximum wind speed (jet core), which can be an important source of turbulence, particularly during the night. Observations at altitude levels ranging from 100 to 200 m (white dashed rectangle in Fig. 2a, b) show the horizontal and vertical wind speed variations. To investigate the nature of this variability in wind speed, we analyzed the maximum wind speed at a fixed altitude of 100 m (jet core) as a function of time (Fig. 2a bottom plot). Figure 2a (bottom plot) shows a sinusoidal oscillation of the wind speed. The vertical wind velocity component (w) within the jet core area shows fluctuation of downward motion (Fig. 2b). A quasi-harmonic oscillation of w is observed in the region characterized by higher wind speed (P-I region in Fig. 2b). Later in time, during P-II, w is found to be chaotic (fluctuation of upward and downward motion). Therefore the variability of the horizontal wind speed components modulates the vertical wind component variability.

To further explore the mechanisms behind the wavy nature of the atmospheric flow characterized by large speed ($U_{(max)}$), the temporal evolution of the temperature (ξ), pressure (P), and $U_{(max)}$ are compared in Fig. 3. Figure 3a shows an exponential decay of temperature with time. The pressure (P) increases until 2136, then decreases. Wavy evolution of the wind speed is clearly seen in Fig. 3c.

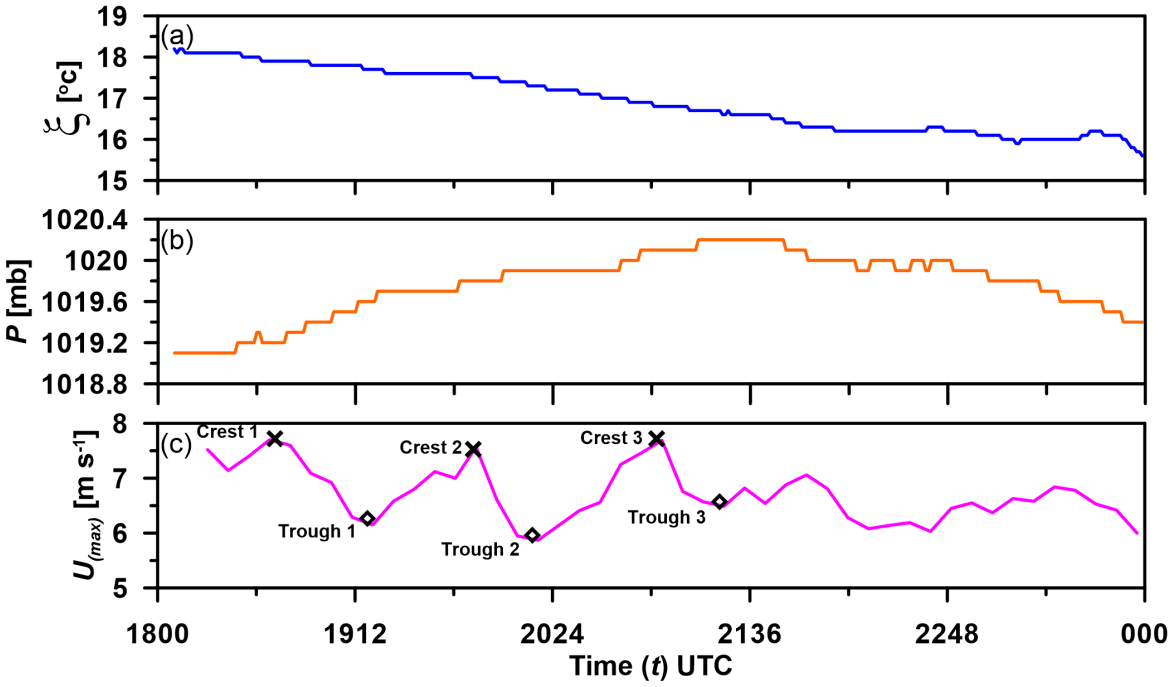

Fig. 3 Temporal variations of (a) temperature [ξ]; (b) Pressure [P] and (c) wind speed [$U_{(max)}$] at 100 m

The study site is characterized by a complex topography with elevated topographic features (50–100 m) perpendicular to the wind. This causes gravity-wave generation and velocity undulation. Other examples given in the literature (e.g., Lott and Teitelbaum 1993; Tsuda 2014; Teixeira 2014; Sandu et al. 2019) and the present observations support the hypothesis that the wavy nature of the wind speed is due to an orographic wave of ~ 60 minutes propagating from east to west. Lott and Teitelbaum (1993) stated that wave packets might be generated within the roughness layer in the temporal domain. Further, Tsuda (2014) stated that the interaction of a sheared wind flow with the topography could be a key parameter for the occurrence of orographic (gravity) waves. In the same year, Teixeira (2014) noted that downstream of the mountains, Lee wave trapping occurs. Owing to wave trapping, the formation of vortices (rotors) can be observed. Recently, Soufflet et al. (2019) showed that for small mountains, trapped Lee waves occur at a small value of the near-surface Richardson number ($Ri = N^2/(\partial U/\partial Z)^2$), where N is the Brunt–Väisälä frequency and U is the horizontal wind speed at height Z. In our case, the value of Ri = 0.0028 estimated, at 100 m altitude a.g.l., reveals the presence of trapped Lee waves. The small value of the inverse Froude number (F_r^{-1}= 0.05) also supports this condition.

3.2 Characteristics of Low-Level Jet

The time-height section of the horizontal wind speed (Fig. 2a) and the RHI radial wind speed (Fig. 2c, d) reveal the presence of low-level jet. The observed wind profiles shown in Figure 4 are in good agreement with Stensrud (1996) and Vera et al. (2006). For a better quantification of the LLJ, we have defined four regions within the boundary layer: the roughness layer, closest to the ground, where there is a constant profile of U; the shear layer; the LLJ jet core, and the upper layer. Three crests and troughs, referred to hereafter as Cr1-3 and Tr1-3, have been selected (Fig. 3c) for assessing the impact of LLJ and gravity waves propagation on turbulence.

The jet speed (U_{max} = 8 m s^{-1}) is similar for these three crests (Cr1-3). As expected, the velocities are smaller (≈ 0.75 × U_{max}) for the trough regions (Tr1-3). A small difference of velocities is observed in the LLJ shear layer region for trough and crest regions (Figs. 4 a–c, blue shading). Moreover, U is nearly similar for Tr1-3 compared to Cr1-3 within the roughness layer. However, the maximum differences of U (for Tr1-3 compared to Cr1-3) are observed in the upper layer and in the jet core.

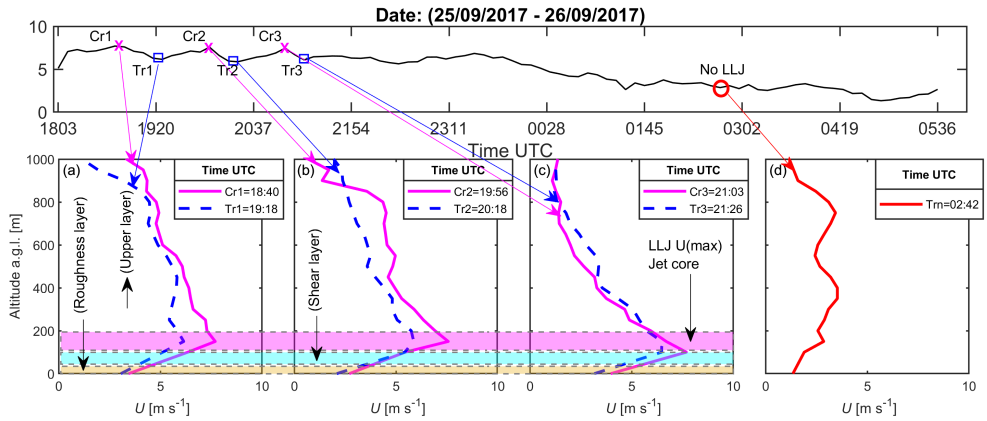

Fig. 4 Vertical profiles of the wind speed U corresponding to three crests and troughs of the propagating gravity wave and low wind conditions; (a) Cr1 and Tr1 (b) Cr2 and Tr2 (c) Cr3 and Tr3, and (d) low wind conditions (no Tr and Cr observed)

In this regard, Storm et al. (2019) stated that the deficiency of vertical mixing might be one of the reasons for the velocity difference in the upper layer compared to the roughness layer. These velocity differences may play an active role in accelerating the wind

speed within the outer layer, unaffected by surface roughness. Furthermore, Figs. 3c and 4 reveal that the gravity wave modulates the wind speed periodically.

3.3 Wind Velocity and Turbulence Assessment near the Ground

Since the primary focus of this study is to evaluate the turbulent properties within the roughness layer, we have analyzed the temporal variations of the velocity vector in the roughness layer using the ultrasonic anemometer data. Figure 5 shows large velocity fluctuations for *u*, *v*, *w* within P-I. These fluctuations are gradually reduced within P-II. This result suggests that larger levels of turbulence are generated during the gravity wave events.

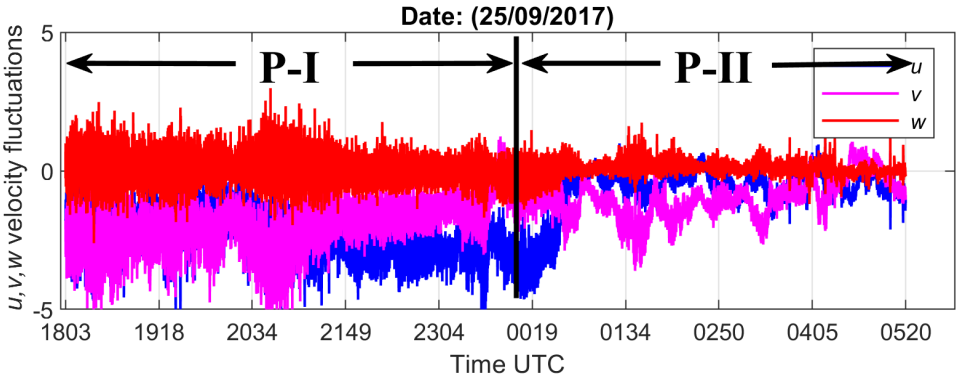

Fig. 5 Time series of *u*, *v*, *w* wind velocity fluctuations (m s^{-1}) in the roughness layer.

Figure 6b–c shows that during the observation period, the dominant wind near the ground was from the north–east. The vertical wind component (*w*) is slightly positive during P-I (w = 0.001 m s^{-1}) and drops to 0.000 during P-II (Fig. 6a). It is also noticed that the wind speed ranges from 3.5 to 4.5 m s^{-1} at P-I while its variation decreases from 1 to 2 m s^{-1}, at P-II (Fig. 6d). The occurrence of larger wind speed at P-I is due to the LLJ.

Figure 6e shows the distribution of Reynolds shear stress R_{uv}, R_{uw}, and R_{vw} as a function of time. It is evident from Fig. 6e that all three shear stress components are negative at P-I and nearly zero at P-II, which is due to a decrease in wind speed during this period. In a coordinate system aligned with the dominant wind direction, that is from east to west, negative R_{uv} values indicate momentum fluxes from north to south, negative R_{uw} values represent momentum fluxes downward, towards the roughness layer. This signifies

that there is a larger magnitude of momentum at P-I, and that the shear layer is a region of turbulence production. Indeed, we observed a relatively high TKE level during P-I. Figure 6e also reveals that the variability of the momentum flux $\overline{u'w'}$ is similar to the maximum wind speed (U) variability shown in Fig. 3c. The gravity wave performs a modulation of the momentum flux, with larger values occurring within crests and lower values within troughs.

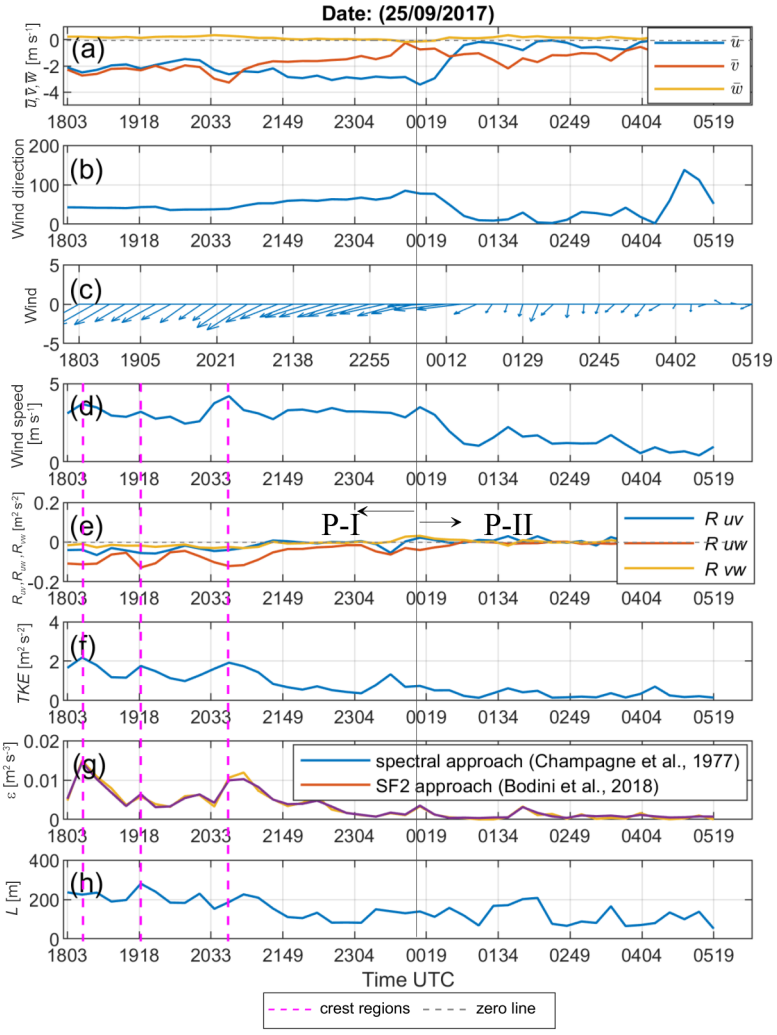

Fig. 6 Time series of (a) u, v, w wind velocity components in the roughness layer, 10-min averaged (m s^{-1}); (b) wind direction with respect to the north; (c) wind velocity vector; (d) horizontal wind speed (m s^{-1}); (e) Reynolds stresses components R_{uv}, R_{uw}, and R_{vw} (m^2 s^{-2}); (f) Turbulence kinetic energy TKE (m^2 s^{-2}); (g) energy dissipation rate ε (m^2 s^{-3}); (h) Turbulent length scale L (m)

311 The temporal variation of TKE (Fig. 6f) shows a similar evolution to that of the wind
312 speed (Fig. 6d), with a variability of ~ 60 minutes during P-I. Thus, the maximum energy
313 appears concentrated at crests and minimum at troughs of the propagating gravity wave.
314 Figure 6g shows the temporal variation of ε. The wavy distribution of ε is evident
315 during P-I. This was revealed for ε estimated by two methods (spectral and SF2 approach).
316 Moreover, the LLJ associated with a gravity wave enhances the turbulent length scale L at
317 P-I (Fig. 6h). Time series of L and ε (Fig. 6g–h) reveal large periodic variations during P-
318 I. Near the ground level, the magnitude of variations of the eddy dissipation and turbulent
319 length scale with respect to the mean value attains 50% and 20% respectively. These
320 variations are caused by the gravity wave propagating at the height of 100 m above the
321 ground. The values of ε deduced from zonal wind component variations by the spectral
322 method and ranging from 0.001 to 0.015 $m^2 s^{-3}$ are found to be analogous to that estimated
323 by the structure function method.
324
325 To ensure the validity of the ε estimation, the power spectral density (PSD) of *u, v,* and
326 *w* velocity components were calculated and their distribution in frequency domain is shown
327 in Fig. 7, for one particular 10-min interval of measurements by sonic anemometer. The
328 distribution shows that the turbulence is isotropic, and the inertial subrange spans from f
329 = 0.1 to 2 Hz (slope -5/3). In this subrange, there is a Richardson–Kolmogorov energy
330 cascade. The turbulent energy is generated in the frequency range $f = 1.5 \times 10^{-2}$ to ~ 0.1
331 Hz. Within the energy-containing range (<0.1 Hz), the energy production is larger for
332 horizontal components *u* and *v* than for the vertical component *w* within the energy-
333 containing range (<0.1 Hz). On the contrary, in the inertial subrange, the energy level of *w*
334 is found slightly larger (Fig. 7). Similar results are obtained for all intervals of
335 measurements at P-I, and demonstrate the dominance of large-scale horizontal and small-
336 scale vertical turbulent motions in the flow field during the observation period (P-I). The
337 direct energy transfer through energy cascading occurs in a smaller band of the inertial
338 subrange (f = 0.1Hz –2 Hz) during P-I, and in a larger band (f = 0.05Hz – 2Hz) during P-
339 II (results not shown).
340

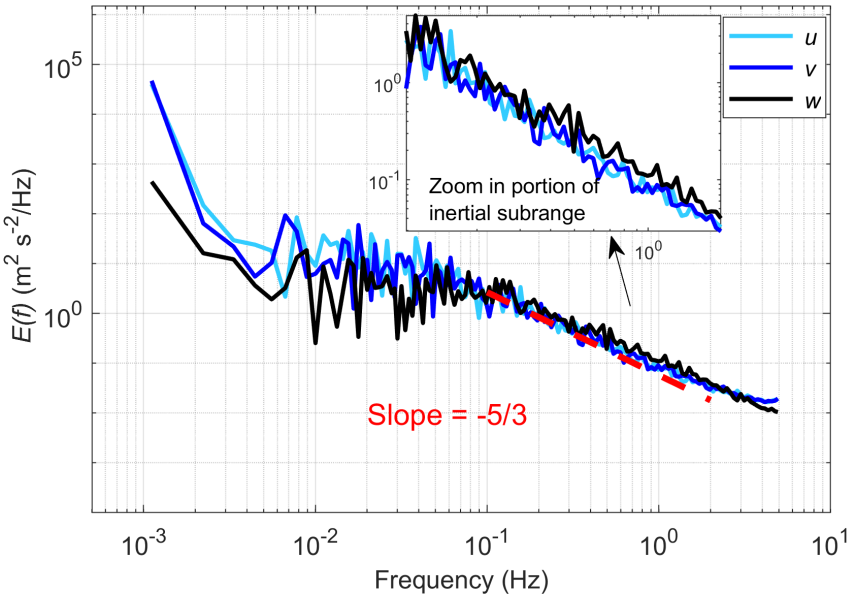

Fig. 7 Power spectral density of three (u, v, w) velocity components recorded by sonic anemometer for 10 min of measurement (1830–1840).

3.4 Assessing Higher-Order Moments and Turbulent Bursting Events

It was shown in Sect. 3.3 that in the roughness layer of the ABL, the shear stress R_{uw} experiences a modulation by the gravity wave. Here we analyze u' and w' time series to better understand the behaviour of their higher-order moments and probability density functions (PDFs). The PDF of u' and w' have been calculated using a method proposed in Tennekes and Lumley (1972). Figure 8 shows that the maximum of the PDF of w' is ~11% larger than that of u', for all the troughs and crests. This means that the probability of occurrence of small fluctuations is larger for the w velocity component than for u. Furthermore, observations show that the peak values of u' and w' distributions at all the troughs are greater than that of at the crests (Fig. 8a). This suggests that the probability of the occurrence of small-scale fluctuations at troughs is larger than at crests. It may be due to the presence of small-scale eddies for lower wind speed in troughs.

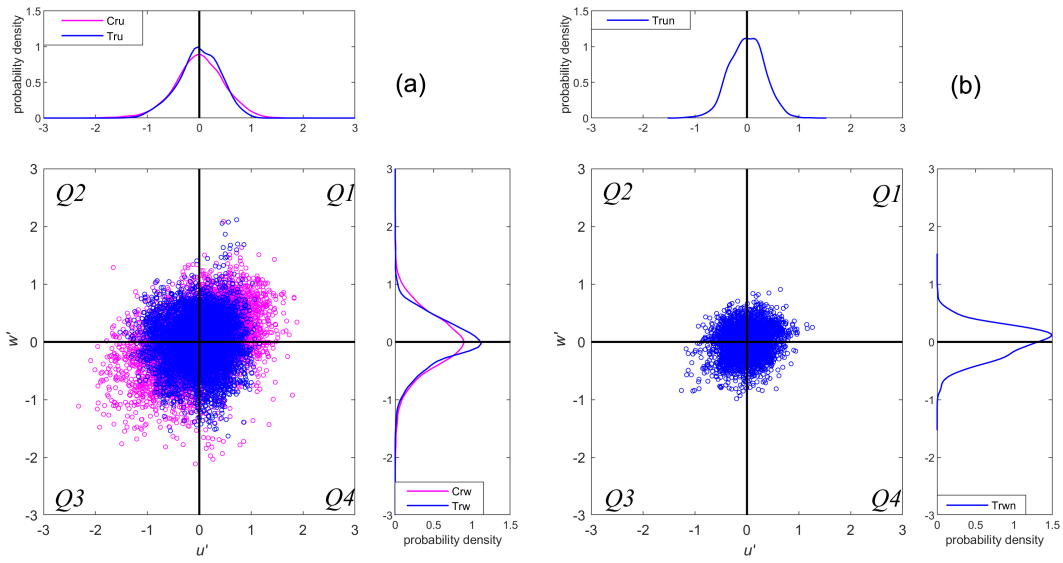

Fig. 8 Scatter plots of u' and w' in four quadrants at the troughs (blue circles) and crests (pink circles) for P-I (a) and P-II (b). The PDF of u' and w' are presented in the top and right side of scatter plots, respectively. The blue circles in (b) do not represent the velocity perturbations since there is no gravity wave at this time

Comparison of panels (a) and (b) in Fig. 8 suggests that the probability of occurrences of small-scale eddies is larger at P-II, without LLJ or gravity wave phenomenon. Wind speed and shear stress are much smaller at P-II than at P-I.

The quadrant analysis has been frequently used to characterize the instantaneous wind speed and its direction of propagation (e.g., Lu and Willmarth 1973; Nakagawa and Nezu 1977; Raupach 1981; Shaw et al. 1983). In the present study, we have used 10-min long time series at each trough and crest region during P-I and P-II. For each time frame, instantaneous u' and w' are plotted in the four quadrants. Distributions of the data (u' and w') in each quadrant represents the behaviour of turbulent bursting events (Nakagawa and Nezu 1977; Raupach 1981). Further, Raupach (1981) stated that the contribution of four events characterizes the total momentum flux ($-R_{uw}$). These events are defined in Fig. 9 as (Q1) ejection event, (Q2) outward interaction, (Q3) sweep event, and (Q4) inward interaction. These events show the direction of propagation of high and low-speed turbulent eddies. In the present study, the quadrant threshold technique is used to define the influences of turbulent events in the flow field and its contribution to the total shear stress $R_{uw} = -\overline{u'w'}$ in the vertical plane (uw).

Figure 8a shows the distribution of the largest amount of data in *Q1* and *Q3* for troughs and crests during P-I. On the contrary, during P-II, an equilibrium in u' and w' distributions in all four quadrants is observed (Fig. 8b). The velocity fluctuations are more spread in *Q1* at crests than the troughs of the gravity wave. The joint distribution of velocity fluctuations shown in Fig. 9 suggests a dominance of low-speed turbulent eddies moving upward (ejection), and high-speed turbulent eddies moving downward (sweep), during the LLJ event. However, turbulence fluctuations are homogeneous for low wind speed ≈ 0.5 m s^{-1} (Fig. 8b). According to Raupach (1981) and Prabha et al. (2008), the contribution of ejection and sweep is larger than inward and outward interactions for LLJ over a large roughness. Their results are in good agreement with those presented in our study. Hunt and Durbin (1999) stated that the occurrence of intense shear shelters by the large eddies within the lower layer leads to the suppression of turbulence. The present measurements were carried out over a flat surface 10 m a.g.l. This weak motion is due to the land proximity. The dominance of low-speed upward turbulent eddies is observed in the presence of a LLJ and gravity waves, with larger undulations for crests than troughs.

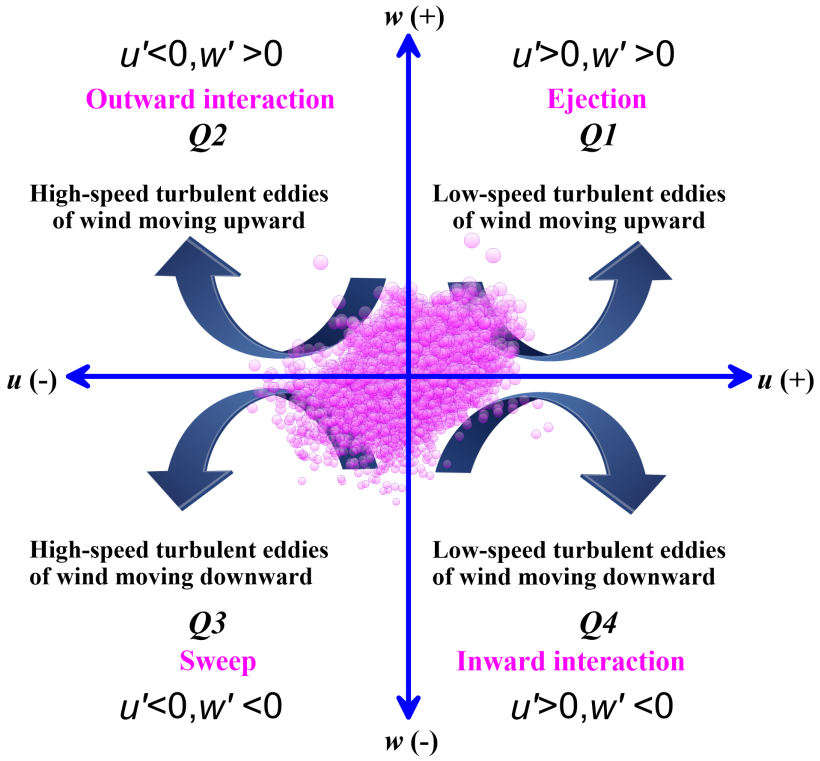

Fig. 9 Definition diagram to portray the characteristics of *u* and *w* velocity fluctuations in the four quadrants

4 Conclusions

Simultaneous measurements of the wind speed by a sonic anemometer and a lidar performed in a coastal region of France were used for assessing flow variability and turbulence in the atmospheric boundary layer. Observations revealed a dominant wind from the north-east (directed from the land towards the sea) and an occurrence of a LLJ in the boundary layer of the lower troposphere, during the first part of the observation period (P-I), which disappeared during the second part (P-II). The wind speed was approximately 7 times higher during P-I, with large periodic variations observed within the roughness layer during this period. We found that these periodic variations were caused by an occurrence of orographic (gravity) waves generated by the wind interactions with the local topography, i.e., limited height coastal relief perpendicular to the wind. To the best of our knowledge, the gravity waves collocated with LLJ have been documented for the first time in the coastal region of northeastern France, sought to be a flat plain with only few raised orographic features.

Our analysis revealed a modulation of turbulence characteristics in the lower ABL (in the vicinity of the ground) by the gravity waves propagating ~100 m above the ground. The major effects of the gravity waves on local turbulence are the following:

1. The generation of a shear stress of zonal and vertical components appeared larger than that of the meridional component. Larger values of the shear stress and downward momentum flux were found within the crests of the propagating wave.
2. The LLJ and the associated gravity wave enhanced the wind turbulence and turbulence kinetic energy dissipation near the ground.
3. Near the ground, the size of turbulent eddies varied in a wide range (from 110 m to 280 m) with respect to the wind speed variation controlled by the gravity wave. The size of turbulent eddies was found larger within the wave's crests, while smaller size turbulent eddies were associated with the troughs.
4. Large-size eddies were found to generate a downward momentum. This enhanced the downward mass transport from the LLJ shear layer to the roughness layer.
5. Assessment of the momentum flux, specifically during the LLJ event, revealed the dominance of low-speed turbulent eddies moving upward (ejection) and high-speed turbulent eddies moving downward (sweep).

We expect that this study is helpful for understanding the boundary-layer dynamics, turbulence, momentum and energy flux variability in the roughness sublayer in the presence of orographic waves. Additionally, turbulence generated by gravity waves may affect aerosol concentrations through turbulent mixing, and thus contribute to a complex dynamics of the aerosols in the ABL.

Acknowledgments The EMPATIE project was funded by the Institut de Recherche Pluridisciplinaire en Sciences de l'Environnement (IRePSE) and the Pôle de Recherche Environnement, Milieux Littoraux et Marins (EMLM) of Université du Littoral Côte d'Opale.

References

Abdullah AJ (1955) The atmospheric solitary wave. Bull Am Meteorol Soc 36(10):511–518

Augustin P, Billet S, Crumeyrolle S, Deboudt K, Dieudonné E, Flament P, Fourmentin M, Guilbaud S, Hanoune B, Landkocz Y, Méausoone C, Roy S, Schmitt FG, Sentchev A, Sokolov A (2020) Impact of Sea Breeze Dynamics on Atmospheric Pollutants and Their Toxicity in Industrial and Urban Coastal Environments. Remote Sensing 12(4):648

Banta RM, Pichugina YL, Newsom RK (2003) Relationship between low-level jet properties and turbulence kinetic energy in the nocturnal stable boundary layer. J Atmos Sci 60(20):2549–2555

Bialkowski SE (1988) Real-time digital filters: infinite impulse response filters. Analytical Chemistry 60(6):403A–13A

Birgitta K (1998) Low level jets in a marine boundary layer during spring. Contribution to Atmospheric Physics 71:359–373

Bodini N, Lundquist JK, Newsom RK (2018) Estimation of turbulence dissipation rate and its variability from sonic anemometer and wind Doppler lidar during the XPIA field campaign. Atmos Meas Tech 11(7): 4291–4308

Bonner WD (1968) Climatology of the Low Level Jet. Mon. Wea. Rev. 96(12):833–850

Bowen BM (1996) Example of Reduced Turbulence during Thunderstorm Outflows. J Appl Meteorol 35(6):1028–1032

Champagne FH, Friehe CA, LaRue JC, Wynagaard JC (1977) Flux measurements, flux estimation techniques, and fine-scale turbulence measurements in the unstable surface layer over land. J Atmos Sci 34(3):515–530

Darby LS, Banta RM, Brewer WA, Neff WD, Marchbanks RD, McCarty BJ, Senff CJ, White AB, Angevine WM, Williams EJ (2002) Vertical Variations in O3 Concentrations before and after a Gust Front Passage. J Geophys Res 107(D13):ACH–9

Droegemeier KK, Wilhelmson RB (1987) Numerical Simulation of Thunderstorm Outflow Dynamics PartI:Outflow SensitivityExperiments andTurbulence Dynamics. J. Atmos.Sci. 44(8):1180–1210

Du Y, Chen G (2019) Heavy rainfall associated with double low-level jets over Southern China. Part II: convection initiation. Mon Weather Rev 147(2):543–565

Eckermann SD, Vincent RA (1993) VHF radar observations of gravity-wave production by cold fronts over southern Australia. J Atmos Sci 50(6):785–806

Fritts DC, Nastrom GD (1992) Sources of mesoscale variability of gravity waves. Part II: Frontal, convective, and jet stream excitation. J Atmos Sci 49(2):111–127

Guest FM, Reeder MJ, Marks CJ, Karoly DJ (2000) Inertia–gravity waves observed in the lower stratosphere over Macquarie Island. J Atmos Sci 57(5):737–752

Hoecker WL (1963) Three Southerly Low-Level Jet Systems Delineated by the Weather Bureau Special Pibal Network of 1961. Mon Weather Rev 91:573–582

Hoffmann L, Xue X, Alexander MJ (2013) A global view of stratospheric gravity wave hotspots located with Atmospheric Infrared Sounder observations. J Geophys Res Atmos 118(2):416–434

Kaimal JC, Finnigan JJ (1994) Atmospheric boundary layer flows: their structure and measurement. Oxford university press

Kallistratova MA, Kouznetsov RD, Kramar VF, Kuznetsov DD (2013) Profiles of wind speed variances within nocturnal low-level jets observed with a sodar. J Atmos Ocean Technol 30(9):1970–1977

Kolmogorov AN (1991) The local structure of turbulence in incompressible viscous fluid for very large Reynolds numbers. Proceedings of the Royal Society of London. Series A: Mathematical and Physical Sciences 434(1890):9–13

Kumer VM, Reuder J, Dorninger M, Zauner R, Grubišić V (2016) Turbulent kinetic energy estimates from profiling wind LiDAR measurements and their potential for wind energy applications. Renew Energy 99:898–910

Lott F, Teitelbaum H (1993) Linear unsteady mountain waves. Tellus a 45(3):201–220

Lu SS, Willmarth WW (1973) Measurements of the structure of the Reynolds stress in a turbulent boundary layer. J Fluid Mech 60(3):481–511

Mitchell MJ, Arritt RW, Labas K (1995) A Climatology of the Warm Season Great Plains Low-Level Jet Using Wind Profiler Observations. Weather Forecast 10(3):576–591

Nakagawa H, Nezu I (1977) Prediction of the contributions to the Reynolds stress from bursting events in open-channel flows. J Fluid Mech 80(1):99–128

Prabha TV, Leclerc MY, Karipot A, Hollinger DY, Mursch-Radlgruber E (2008) Influence of nocturnal low-level jets on eddy-covariance fluxes over a tall forest canopy. Boundary-Layer Meteorol 126(2):219–236

Plougonven R, Teitelbaum H (2003) Comparison of a large‐scale inertia‐gravity wave as seen in the ECMWF analyses and from radiosondes. Geophys Res Lett 30(18):1–4

499 Ruchith RD, Raj PE (2015) Features of nocturnal low level jet (NLLJ) observed over a tropical Indian station
500 using high resolution Doppler wind lidar. Journal of Atmospheric and Solar-Terrestrial Physics 123:113–
501 123
502 Raupach MR (1981) Conditional statistics of Reynolds stress in rough-wall and smooth-wall turbulent
503 boundary layers. J Fluid Mech 108:363–382
504 Raupach M, Finnigan JJ, Brunet Y (1996) Coherent eddies and turbulence in vegetation canopies: the mixing-
505 layer analogy. Boundary-Layer Meteorol 25:351–382
506 Rinne H (2010) Location-scale distributions—Linear estimation and probability plotting using MATLAB.
507 Justus–Liebig–Univ., Dept. of Economics and Management Science, Giessen, Germany
508 Rotach MW, Calanca P (2015) Boundary layer (atmospheric) and air pollution | Microclimate. Encyclopedia
509 of atmospheric sciences 1:258–264
510 Sandu I, van Niekerk A, Shepherd TG, Vosper SB, Zadra A, Bacmeister J, Beljaars A, Brown AR, Dörnbrack
511 A, McFarlane N, Pithan F (2019) Impacts of orography on large-scale atmospheric circulation. npj
512 Climate and Atmospheric Science 2(1):1–8
513 Shaw RH, Tavangar J, Ward DP (1983) Structure of the Reynolds stress in a canopy layer. Journal of climate
514 and applied meteorology 22(11):1922–31
515 Schmitt F, Schertzer D, Lovejoy S, Brunet Y (1994) Empirical study of multifractal phase transitions in
516 atmospheric turbulence. Nonlin Process Geophys 1: 95–104
517 Smedman AS, Högström U, Hunt JC (2004) Effects of shear sheltering in a stable atmospheric boundary
518 layer with strong shear. Q J R Meteorol Soc 130(596):31–50
519 Soufflet C, Lott F, Damiens F (2019) Trapped mountain waves with a critical level just below the surface. Q
520 J R Meteorol Soc 145:1503–1514
521 Stensrud DJ (1996) Importance of low-level jets to climate: A review. J Clim 9(8):1698–711
522 Storm B, Dudhia J, Basu S, Swift A, Giammanco I (2009) Evaluation of the weather research and forecasting
523 model on forecasting low ‐ level jets: Implications for wind energy. Wind Energy: An International
524 Journal for Progress and Applications in Wind Power Conversion Technology 12(1):81–90
525 Taylor GI. Statistical theory of turbulence. IV (1935) Diffusion in a turbulent air stream. Proceedings of the
526 Royal Society of London. Series A-Mathematical and Physical Sciences 151(873):465–78
527 Teixeira MA (2014) The physics of orographic gravity wave drag. Frontiers in Physics 2(43) : 1–24
528 Tennekes H, Lumley JL, Lumley JL (1972) A first course in turbulence. MIT press
529 Tepper M (1950) A proposed mechanism of squall lines: The pressure jump line. J Meteorol 7(1):21–29
530 Tsuda T (2014) Characteristics of atmospheric gravity waves observed using the MU (Middle and Upper
531 atmosphere) radar and GPS (Global Positioning System) radio occultation. Proceedings of the Japan
532 Academy, Series B. 90(1):12–27
533 Uccellini LW, Koch SE (1987) The synoptic setting and possible energy sources for mesoscale wave
534 disturbances. Mon Weather Rev 115(3):721–9

Vaughan G, Hooper D (2015) Mesosphere–Stratosphere–Troposphere and Stratosphere–Troposphere Radars and Wind Profilers. Encyclopedia of Atmospheric Sciences Second Edition (1): 29–437

Vera C, Baez J, Douglas M, Emmanuel CB, Marengo J, Meitin J, Nicolini M, Nogues-Paegle J, Paegle J, Penalba O, Salio P (2006) The South American low-level jet experiment. Bull Am Meteorol Soc 87(1):63–78

Wei W, Zhang HS, Schmitt FG, Huang YX, Cai XH, Song Y, Huang X, Zhang H (2017) Investigation of Turbulence behaviour in the stable boundary layer using arbitrary-order Hilbert spectra. Boundary-Layer Meteorol. 163(2):311–26

Whiteman CD, Bian X, Zhong S (1997) Low-Level Jet Climatology from Enhanced Rawinsonde Observations at a Site in the Southern Great Plains. J Appl Meteorol 36(10):1363–1376

Zhong S, Fast JD, Bian X (1996) A Case Study of the Great Plains Low-Level Jet Using Wind Profiler Network Data and a High-Resolution Mesoscale Model. Mon Weather Rev 124(5):785–806